Eur. Phys. J. Plus (2020) 135:734
https://doi.org/10.1140/epjp/s13360-020-00745-6

THE EUROPEAN PHYSICAL JOURNAL PLUS

Regular Article

Structures, stabilities and electronic properties of $Ti_mSi_n^-$ ($m = 1$–2, $n = 14$–20) clusters: a combined ab initio and experimental study

Xue Wu[1], Qiuying Du[1], Si Zhou[1], Xiaoming Huang[2], Maodu Chen[1], Lin Miao[3], Guangjia Yin[3], Jiashuai Wang[3], Kai Wang[3], Bernd von. Issendorff[4], Lei Ma[3,a], Jijun Zhao[1,b]

[1] Key Laboratory of Materials Modification by Laser, Ion and Electron Beams (Dalian University of Technology), Ministry of Education, Dalian 116024, China
[2] School of Ocean Science and Technology, Dalian University of Technology, Panjin Campus, Panjin 124221, China
[3] Tianjin International Center of Nanoparticles and Nanosystem, Tianjin University, Tianjin 300072, China
[4] Department of Physics and FMF, University of Freiburg, 79104 Freiburg, Germany

Received: 9 July 2020 / Accepted: 2 September 2020 / Published online: 16 September 2020

Abstract Titanium-doped silicon clusters anions, $Ti_mSi_n^-$ ($m = 1$–2, $n = 14$–20), have been investigated by photoelectron spectroscopy and density functional theory (DFT) calculations. Low-energy structures of $Ti_mSi_n^-$ clusters have been globally searched using a genetic algorithm combined with DFT calculations. The electronic density of states and vertical detachment energies have been computed at the HSE06/aug-cc-pVDZ level and compared to the experimental data. Excellent agreement is found between theory and experiment especially in case of the singly doped clusters. In general, clusters with size $m+n \leq 17$ prefer cage structures, while larger sized clusters evolve on a quasi-fullerene $Ti@Si_{14}$ structural motif. Natural population analysis reveals that the Ti atoms possess negative charges and thus act as electron acceptors. The calculated binding energies and HOMO–LUMO gaps show that the clusters with cage structures have significantly higher stability, particularly $Ti_1Si_{16}^-$ and $Ti_2Si_{15}^-$. One reason is that neutral Ti_2Si_{15} exhibits a closed-shell electronic structure as a superatom, like Ti_1Si_{16}.

1 Introduction

The continuous miniaturization of silicon-based electronic devices has stimulated intensive explorations of the electronic properties of silicon-based nanostructures. Silicon nanoclusters have attracted enormous attention in the past three decades as promising building blocks for self-assembled structures in the microelectronics industry. Their physical and chemical properties can be tailored by cluster size and geometry [1–6]. However, with the preferential

Electronic supplementary material The online version of this article (https://doi.org/10.1140/epjp/s13360-020-00745-6) contains supplementary material, which is available to authorized users.

[a] e-mail: maleixinjiang@tju.edu.cn
[b] e-mail: zhaojj@dlut.edu.cn (corresponding author)

sp^3 bonding nature, Si clusters inevitably have surface dangling bonds, which makes it difficult to form very stable structures [7]. Doping metal atoms into Si clusters is an effective strategy to stabilize the cluster structure and also tailor the cluster properties [1]. For instance, the cage-like cluster Si_{16} encapsulating a Ti atom was demonstrated to be one of the most stable Si-based clusters [8–10]. It was first predicted theoretically in 2001 by Kumar and Kawazoe [4], and recently synthesized by Nakajima's group on a macroscopic scale based on a clean dry-physical process [11]. Ti atom doping induces a large HOMO–LUMO gap of 1.90 eV [12], giving the clusters potential for applications in electronics, optoelectronics and optics. Si clusters doped by other metal atoms such as Sc, V, Cr, Zr, and Hf have also been theoretically studied and produced in the laboratory [12–15].

To date, Si clusters doped by a single Ti atom ($Ti_1@Si_n$) have been extensively investigated, including their atomic structures [16–20], stability [21, 22], electronic, catalytic [23] and optical properties for a wide range of cluster size [6, 9, 24–26]. The mass spectra showed that neutral Ti_1Si_{16} is a "magic number" with high abundance [12], while in the mass spectra of anions both Ti_1Si_{15} and Ti_1Si_{16} clusters exhibit high intensities [27]. Koyasu et al. measured the HOMO–LUMO gap of the Ti_1Si_{16} cluster to be ~ 1.90 eV by photoelectron spectroscopy [12, 28]. In addition, mass spectrometry, photoelectron spectroscopy and adsorption reactivity toward H_2O demonstrated that the neutral $M_1@Si_n$ (M = Ti, Zr and Hf) clusters possess highest stability at $n = 16$ due to closed electronic shells and highly symmetric geometries [15, 29].

On the theoretical side, putative ground state geometries of neutral $Ti_1@Si_n$ clusters have been determined. The clusters tend to form basket structures with n up to 12, while the cage structure becomes favorable for $n \geq 13$. The binding energy increases with the cluster size, and attains a maximum for $n = 16$ [16, 17]. For $Ti_1@Si_n$ clusters with $n > 16$, the excess Si atoms aggregate into an apical bud [18, 30]. Koyasu et al. [12] conjectured that the high stability of $Ti_1@Si_{16}$ is attributed to a 20-electron shell closing by parts of the valence electrons, which were assumed to behave like a nearly free electron gas inside the Si cage [31, 32]. Later, Torres et al. emphasized that all 68 valence electrons produce a shell closing [33, 34]. The bulk materials assembled from $Ti_1@Si_{16}$ clusters can exhibit high-temperature superconducting properties [9]. Also, a linear heterotrimer of the fullerene-like $M_1@Si_{16}$ (M = Sc, Ti and V) clusters was shown to have a large dipole moment [25], potentially suitable for optoelectronics such as silicon-based lasers, tagging and photoexcitation.

Despite the aforementioned achievements, the knowledge on the structural and physical properties of Ti-doped Si clusters with sizes other than $n = 16$ is still limited. Especially, Si clusters doped by multiple Ti atoms remain unexplored. Here we carried out density functional theory (DFT) calculations combined with experimental photoelectron spectroscopy to elucidate the structure, stability and electronic properties of mono- and bi-doped Si cluster anions $Ti_mSi_n^-$ ($m = 1, 2$) with sizes $n = 14$–20. The low-energy isomer structures of $Ti_mSi_n^-$ were searched and the ground state structures were determined by comparing the computed photoelectron spectra with the experimental ones. The electronic structures of Ti-doped Si clusters were examined to identify the isomers with superatomic character. These theoretical and experimental results establish a comprehensive picture of the structure, stability and electronic properties of the low-energy isomers of Ti-doped Si clusters as a function of cluster size and help to identify building blocks for novel self-assembled silicon-based nanomaterials.

2 Experimental and theoretical methods

2.1 Experimental

Silicon and silicon-metal alloy clusters were produced in a magnetron sputtering gas aggregation cluster source. Silicon and metal atoms were sputtered from a 2-inch target (a sandwich of a silicon target with holes drilled into it in the sputtering region and a titanium target) into a mixture of helium and argon (flux ratio roughly 3:1) with a total pressure of around 0.5 mbar inside a liquid nitrogen cooled aggregation tube. Under these conditions Si atoms condenses into Si and Si alloy clusters with various sizes. The high density of charge carriers yielded by the magnetron discharge led to effective charging of the clusters forming both anions and cations. The clusters then expanded with the buffer gas through an adjustable iris into vacuum. A radio-frequency (RF) octupole ion guide steered the cluster anions into the next chamber where they were fed into a RF 12-pole cryogenic ion trap. In this trap, which was cooled to 80 K, the clusters were thermalized by collisions with precooled helium buffer gas with a pressure of about 10^{-3} mbar. Bunches of cluster anions were then extracted from the trap and introduced into a high resolution, double reflection time-of-flight mass spectrometer, where a multiwire mass gate located at the focal point of the first reflector would select a specific mass with a resolution of about $m/\Delta m = 2000$. The size-selected clusters then were reflected and rebunched again by the second reflector, and decelerated by a pulsed electric field. After that, the clusters entered into the interaction region of a magnetic bottle time-of-flight photoelectron spectrometer, where they were irradiated by a laser pulse from a KrF excimer laser. Typically, photoelectron spectra (PES) were averaged over 30,000 laser shots at a repetition rate of 100 Hz. The spectrometer was calibrated by measuring the known PES of platinum anions, thereby leading to an error of the measured binding energies of less than 30 meV. The mass spectrum ensured there is no silicon oxides contributed to the PES signal (Fig. S1 of Supporting Information).

2.2 Theoretical

The low-energy isomer structures of $Ti_mSi_n^-$ ($m = 1$–2, $n = 14$–20) clusters were searched independently by an unbiased comprehensive genetic algorithm (CGA) code [35], which is implemented within the DMol^3 program [36]. The validity and efficiency of this CGA-DFT scheme have been well demonstrated in a series of our recent studies on Si [37, 38], B [39, 40], V–Si [13, 41], B–Si [42], Ti/Zr/Hf–Si [43], Fe–Ge [44] Cr–Ge [45] and Mo–B [46] clusters. Further details of CGA can be found in our recent review article [35]. For each cluster size, a few independent CGA searches were performed with different presumed symmetries, including the C_1, C_2, C_3, and C_s point groups. With each specific symmetry constraint, every CGA search ran at least 3000 iterations and retained 16 members in the population. The mutation ratio was set as 30% to ensure the diversity of population. The resulting child clusters were optimized by DMol^3 using the double numerical basis including d-polarization function (DND) and the Perdew–Burke–Enzerhof (PBE) functional within the generalized gradient approximation (GGA) [47, 48].

The energetic and electronic properties of the $Ti_mSi_n^-$ clusters obtained from CGA-DFT search were further calculated by the Gaussian09 program [49] using the aug-cc-pVDZ basis set [50] and HSE06 functional [51]. Our recent benchmark study [38] demonstrated that this methodology can provide accurate description of the structural and electronic properties for Si_n clusters with $n = 14$–20. For comparison, we also optimized the structures of all the considered isomers using the PBE0 functional [52]. For each cluster size, the relative energies

of isomers predicted by these two functionals are nearly identical with a discrepancy less 0.02 eV (see Figs. S2, S3 of Supporting Information). Vibrational analysis were carried out to ensure that there is no imaginary frequency corresponding to the saddle point on potential energy surface and the zero-point-energy (ZPE) was included in the final energy. Spin multiplicities testing show that doublet for $Ti_mSi_n^-$ anions is most stable state, and singlet and triplet for neutral species may appear as most stable state.

The stability of a $Ti_mSi_n^-$ cluster can be characterized by the binding energy (E_b) defined as:

$$E_b\left(Ti_mSi_n^-\right) = \left[nE(Si) + E\left(Ti^-\right) + (m-1)E(Ti) - E\left(Ti_mSi_n^-\right)\right]/(m+n),$$

where $E(Ti_mSi_n^-)$ is the energy of the anionic $Ti_mSi_n^-$ cluster; E(Si), $E(Ti^-)$ and E(Ti) are the energies of an individual Si atom, Ti^- anion and Ti atom, respectively. The natural population analysis (NPA) [53] of $Ti_mSi_n^-$ was conducted using the natural bond orbital (NBO) 3.1 program [54, 55] implemented in the Gaussian09 package.

To quantitatively compare with the experimental results, the vertical detachment energy (VDE) was calculated as the energy required to remove an electron from the highest occupied molecular orbital (HOMO) without relaxing the atomic configuration, which corresponds to the first peak maxima of the photoelectron spectrum. Upon photoemission, the structure of the neutral Ti_mSi_n cluster remains identical to that of the anion under the assumption of a vertical transition. The PES of anionic clusters were simulated using the 'generalized Koopman's theorem' based on the energy levels from DFT calculations [56]. For the VDEs of deeper Kohn–Sham states, we shifted the calculated DOS globally in order to align the binding energy of the HOMO with the theoretical VDE value [57, 58]. Each line of the Kohn–Sham eigenvalue spectrum was broadened by a Gaussian function of width 0.06 eV.

3 Results and discussion

3.1 Structures and stability of $Ti_mSi_n^-$

The low-energy isomers of $Ti_mSi_n^-$ anions globally searched by the CGA-DFT procedure are displayed in Figs. S2, S3 of Supporting Information. For each $Ti_mSi_n^-$ cluster system, we considered only the isomers with energies higher than the ground state by less than 0.20 eV, which are shown in Fig. 1 and denoted as n–I, n–II, n–III, and so on (from the lowest to highest energies). The relative stabilities of various isomers are given by Table 1.

3.1.1 $Ti_1Si_n^-$

For the mono-doped anionic Si clusters, Ti atoms are encapsulated in the center of Si cages (Fig. 1a). The smaller-sized $Ti_1Si_n^-$ clusters (n= 14–16) prefer simple cage structures. In particular, the lowest-energy isomers of $Ti_1Si_{14}^-$ and $Ti_1Si_{15}^-$ adopt a bicapped pentagonal prism as the structural motif, with two and three Si atoms inserted on the waist of prism showing C_{2v} and C_s symmetry, respectively. These are consistent with the structures reported by Reveles and Khanna [31] Both $Ti_1Si_{14}^-$ and $Ti_1Si_{15}^-$ have another isomer with energy higher than the ground state of only 0.01 and 0.09 eV, respectively. The 14–II isomer has a Si dimer hanging on a tetragon face of a hexagonal prism and therefore only has C_s symmetry, while 15–II is a basket-like structure with C_{2v} symmetry. 14–III, 14–IV and 14–V are higher in energy than the ground state by 0.01, 0.09 and 0.12 eV, respectively, with two silicon atoms hanging on a C_{3v} Ti@Si_{12} motif. The $Ti_1Si_{16}^-$ cluster has three low-lying isomers:

Table 1 Relative energy (ΔE), binding energy per atom (E_b), HOMO–LUMO gap (E_{HL}) and VDE of the isomers of $Ti_mSi_n^-$ ($m = 1$–2, $n = 14$–20) clusters by HSE06/aug-cc-pVDZ calculations

Isomer		ΔE (eV)	E_b (eV)	E_{HL}(eV)	VDE (eV)	
					Cal.	Expt.
$Ti_1Si_{14}^-$	14–I	0.00	5.09	2.50	4.26	4.31(6)
	14–II	0.01	5.09	1.29	3.12	
	14–III	0.01	5.09	1.86	3.64	
	14–IV	0.09	5.09	1.47	3.33	
	14–V	0.12	5.09	1.16	3.46	
$Ti_1Si_{15}^-$	15–I	0.00	5.13	1.88	3.59	3.66(6)
	15–II	0.09	5.13	1.26	3.21	
$Ti_1Si_{16}^-$	16–I	0.00	5.13	0.75	2.20	2.35(6)
	16–II	0.06	5.13	0.88	2.32	
	16–III	0.10	5.12	1.47	3.48	
$Ti_1Si_{17}^-$	17–I	0.00	5.11	0.82	3.14	3.15(6)
	17–II	0.07	5.10	0.73	3.06	
$Ti_1Si_{18}^-$	18–I	0.00	5.12	1.14	3.24	3.27(6)
$Ti_1Si_{19}^-$	19–I	0.00	5.12	1.23	3.48	3.49(6)
$Ti_1Si_{20}^-$	20–I	0.00	5.13	0.91	3.10	–
	20–II	0.16	5.12	1.25	3.53	
$Ti_2Si_{14}^-$	14–I	0.00	5.19	1.38	3.27	3.04(6)
	14–II	0.08	5.18	1.51	3.17	
	14–III	0.11	5.18	1.43	3.05	
$Ti_2Si_{15}^-$	15–I	0.00	5.18	1.28	3.31	2.98(6)
	15–II	0.01	5.18	1.44	2.91	
	15–III	0.19	5.17	1.42	3.04	
$Ti_2Si_{16}^-$	16–I	0.00	5.18	1.25	3.44	3.40(6)
	16–II	0.12	5.17	1.02	3.09	
$Ti_2Si_{17}^-$	17–I	0.00	5.17	0.96	3.32	3.32(6)
	17–II	0.20	5.16	0.95	3.24	
$Ti_2Si_{18}^-$	18–I	0.00	5.17	1.18	3.57	3.57(6)
	18–II	0.17	5.16	1.13	3.52	
$Ti_2Si_{19}^-$	19–I	0.00	5.18	0.94	3.46	–
	19–II	0.03	5.18	1.06	3.60	
$Ti_2Si_{20}^-$	20–I	0.00	5.19	0.73	3.50	–
	20–II	0.01	5.19	1.44	3.89	
	20–III	0.02	5.19	1.06	3.53	

The uncertainties in the experimental VDEs are given in parentheses

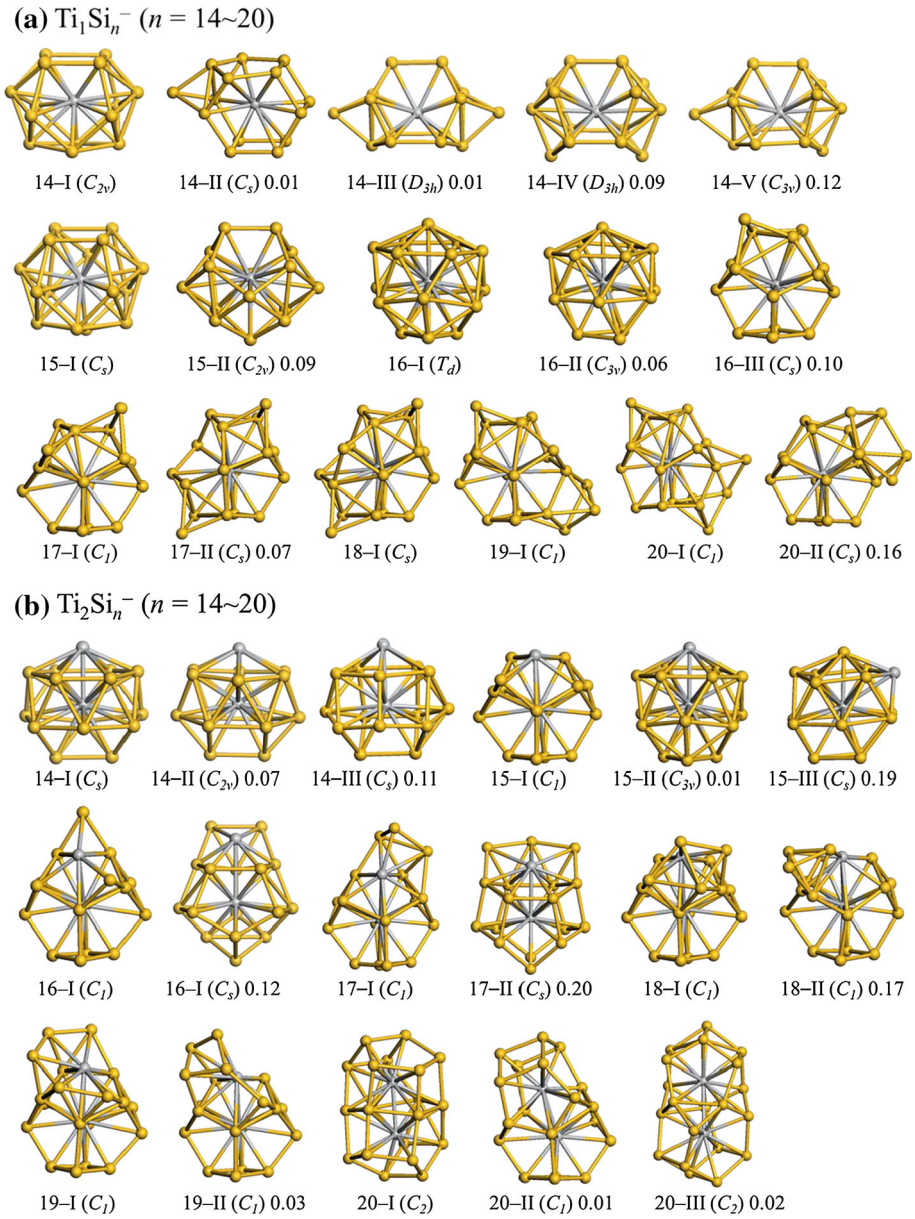

Fig. 1 Low-energy structures of $Ti_mSi_n^-$ (m = 1–2, n = 14–20) clusters discovered using HSE06/aug-cc-pVDZ. For each cluster size, several low-energy isomers marked as n–I, n–II, and n–III. The Si and Ti atoms are shown in gold and silver colors, respectively. The cluster symmetry is given in bracket and the energy difference (in eV) relative to the ground state is provided

the Frank–Kasper (FK) polyhedron structure with T_d symmetry [59], a distorted FK structure with C_{3v} symmetry [43], and a Ti@Si_{14} capped with a Si_2 dimer with C_s symmetry [4]. The former two isomers are nearly degenerate with an energy difference of only 0.06 eV, while the latter one is higher in energy than the ground state by 0.10 eV.

A fullerene-like D_{3h} structure of Ti@Si_{14} (hereafter denoted as Ti@Si_{14}), which can be viewed as a tertruncated square bipyramid, serves as the structure motif of the larger $Ti_1Si_n^-$ cluster. Similar to the carbon fullerenes with pentagonal and hexagonal faces, its outer Si_{14} cage contains three tetragonal faces and six pentagonal faces with each Si atom being tri-coordinated. According to the Euler theorem, 18, 16, 14, 12 and 10-vertex polyhedrons could have 1, 2, 3, 4 and 5 tetragonal faces and 10, 8, 6, 4 and 2 pentagonal faces, respectively. Analogous to the isolated pentagon rule for carbon fullerene, the D_{3h} Si_{14} cage can be regarded as the smallest "quasi-fullerene" obeying the "isolated tetragon rule". For larger cluster anions ($n=$ 17–20), the D_{3h} Ti@Si_{14} served as the structural motif is capped with various apical buds by the excess Si atoms. The $Ti_1Si_{17}^-$ cluster has two low-lying isomers with an energy difference of 0.07 eV, featured as three Si atoms capping one pentagon face or two adjacent pentagon faces of the Ti@Si_{14} motif, respectively. The clusters with $n=$ 18–19 have only one low-lying isomer within the considered energy range: $Ti_1Si_{18}^-$ with C_s symmetry can be derived by one Si atom capping a hexagonal face of the 17–II isomer; $Ti_1Si_{19}^-$ with low symmetry has a Si dimer capping a pentagon face of the Ti@Si_{14} motif, and three Si atoms capping the pentagon of the other side. The $Ti_1Si_{20}^-$ cluster has two low-lying isomers with an energy difference of 0.16 eV. The 20–I isomer can be derived by adding one Si atom onto the 19–I isomer, and 20–II isomer with C_s symmetry has six Si atoms capping a pentagon of the Ti@Si_{14} motif.

3.1.2 $Ti_2Si_n^-$

For the bi-doped anionic Si clusters, one Ti atom is encapsulated in the center of Si cages, while the other Ti atom stays on the cluster surface bonding with several Si atoms (Fig. 1b). The $Ti_2Si_{14}^-$ cluster has a cage structure, while for $n=$ 15–20, the Ti@Si_{14}-based structural motif starts to dominate the low-lying isomers. Specifically, the $Ti_2Si_{14}^-$ cluster has three low-lying isomers. The two lowest isomers are nearly degenerate with an energy difference of 0.08 eV. They can be viewed as a Ti@Si_{12} motif with the hexagonal antiprism capped by one Ti atom and one Si dimer, respectively, giving either C_s or C_{2v} symmetry. The 14–III isomer with C_s symmetry is higher in energy by 0.11 eV than the lowest-energy one. For $n=$ 15, the lowest-energy isomer can be derived by capping a Si–Ti dimer onto a pentagon face of the Ti@Si_{14}^- motif. The other two isomers are the FK and distorted FK polyhedrons with C_{3v} and C_s symmetry, respectively, and are higher in energy than the ground state by 0.01 and 0.19 eV, respectively. As we will discuss in detail later, the FK isomer with C_{3v} symmetry is a probable candidate for the structure present in the experiment. As the cluster size increases, the excess Si atoms start to evolve into a bud or sub-cage enclosing the Ti atom on the cluster surface.

For larger cluster anions ($n=$ 17–20), most isomers have a Ti@Si_{14}-based structure. In particular, the $Ti_2Si_n^-$ clusters with $n=$ 16, 17 and 18 can be viewed as the Ti@Si_{14} motif with two, three and four Si atoms capping a pentagon face surrounding the surface Ti atom, respectively. $Ti_2Si_{16}^-$, $Ti_2Si_{17}^-$ and $Ti_2Si_{18}^-$ have two other isomers higher in energy by 0.12, 0.20 and 0.17 eV than the ground state ones, respectively. 16–II and 18–II have a $TiSi_2$ triangle and a $TiSi_4$ trigonal bipyramid capping a pentagon face of the Ti@Si_{14} motif, while 17–II is a fourteen-vertex cage capped by a $TiSi_3$ rhombus with C_s symmetry. The $Ti_2Si_{19}^-$ cluster has two low-lying isomers with an energy difference of 0.03 eV, which can be viewed as five Si atoms capping a pentagon face of the Ti@Si_{14} motif and surrounding the surface Ti atom. The $Ti_2Si_{20}^-$ cluster has three low-lying isomers within an energy range of 0.02 eV. They all have fused cages encapsulating the two Ti atoms. More specifically, the 20–I and 20–III isomers present two identical 13-vertex cages sharing six Si atoms with C_2 symmetry.

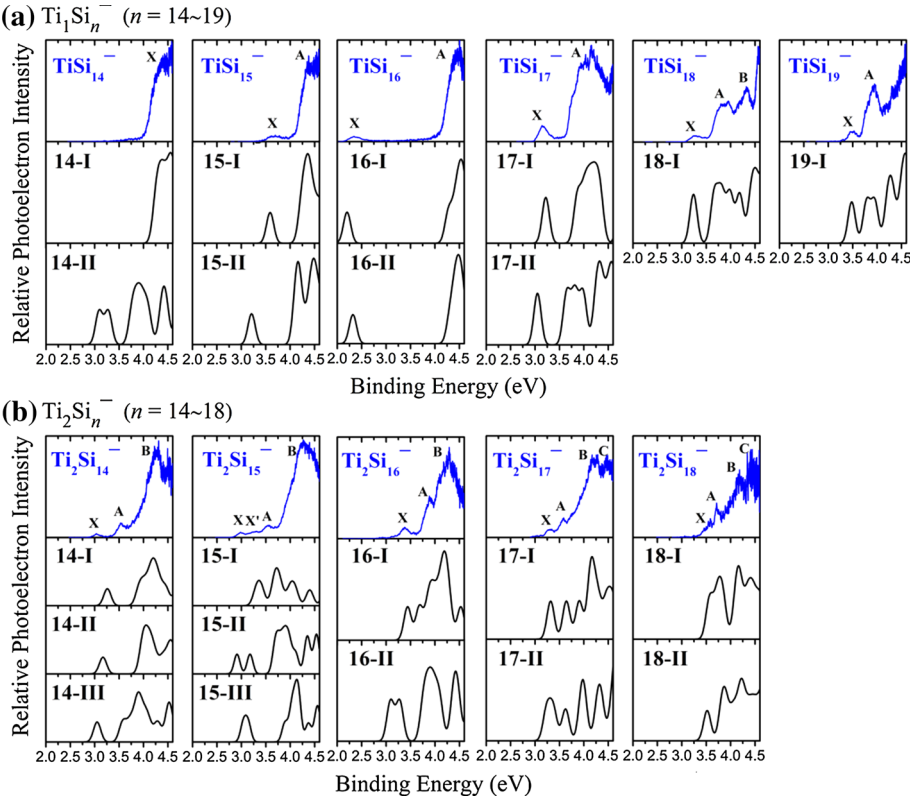

Fig. 2 Photoelectron spectra of low-lying isomers of $Ti_mSi_n^-$ ($m = 1$–2, $n = 14$–20) from experiment (blue lines) and theory (black lines). In the simulations, Gaussian broadening with a width of 0.06 eV is used

The 20–II isomer has the $Ti@Si_{14}$ motif and a 10-vertex cage fused by sharing a Ti atom and three Si atoms.

3.2 Photoelectron Spectra of $Ti_mSi_n^-$

The experimental PES of $Ti_mSi_n^-$ ($m = 1$–2, $n = 14$–20) clusters recorded with 248 nm photons are given in Fig. 2 (blue lines), compared with the computed spectra (black lines). As the anions are open-shell with a single unpaired electron, both singlet and triplet final states have been taken into consideration in the simulated PES. The VDE values, representing the vertical binding energy of an excess electron to the corresponding neutral cluster, are plotted in Fig. 3.

For $Ti_1Si_{14}^-$, the experimental spectrum has one characteristic peak corresponding to the ground state transition X with VDE = 4.31 eV (Fig. 2a). The simulated PES of the 14–I isomer shows one major peak centered at 4.26 eV, while the 14–II isomer shows multiple peaks, significantly deviating from the experimental spectrum. Thus, the 14–I isomer is the most probable structure detected in the experiment. For $Ti_1Si_{15}^-$, $Ti_1Si_{16}^-$ and $Ti_1Si_{17}^-$, the experimental spectrum presents a low-intensity X band with VDE values of 3.66, 2.35 and 3.15 eV, and a prominent A band centered at 4.32, 4.48 and 4.20 eV, respectively. Particularly, $Ti_1Si_{16}^-$ shows a large gap of 1.97 eV between the X band and A band, which

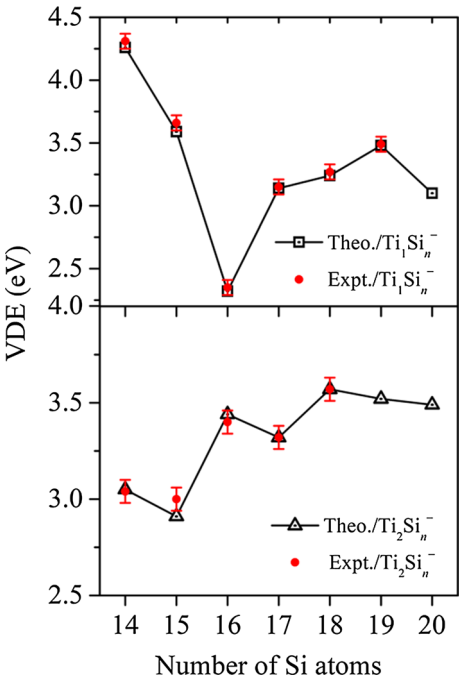

Fig. 3 VDEs of $Ti_mSi_n^-$ ($m=$ 1–2, $n=$ 14–20) clusters as a function of n. Red dots: experimental values with error bars; black squares: calculated results for $m=1$; black triangles: calculated results for $m=2$, in which the calculated VDEs of $Ti_2Si_{14}^-$ and $Ti_2Si_{15}^-$ come from their third and second isomer, respectively

is the HOMO–LUMO gap of the neutral Ti_1Si_{16} cluster with X and A bands corresponding to photodetachment of an electron from the singly occupied molecular orbital (SOMO) of the $Ti_1Si_{16}^-$ anion and from the HOMO of the neutral Ti_1Si_{16} species, respectively. The simulated PES of 15–I, 16–II and 17–I isomers have a prominent peak at 4.38, 4.49 and 4.22 eV, and a minor peak at 3.59, 2.32 and 3.14 eV, respectively, in good agreement with the experimental data for each size. In contrast, the 16–I isomer has a lower VDE (2.20 eV), and the 15–II and 17–II isomers exhibit multiple peaks in the A band; hence they can be excluded from the clusters obtained in the laboratory. For $Ti_1Si_{18}^-$ and $Ti_1Si_{19}^-$, the experimental spectrum has a low-intensity X band at 3.27 and 3.49 eV, respectively, followed by multiple peaks above 3.90 eV corresponding to A and B bands. The computed PES well reproduce the features of the experimental spectra, showing X bands at 3.24 and 3.48 eV for $Ti_1Si_{18}^-$ and $Ti_1Si_{19}^-$, and prominent A bands with several overlapping peaks, respectively. Therefore, for the mono-Ti-doped anionic Si clusters, the lowest-energy isomers found by CGA are usually the structures obtained in the experiment, with the exception of $Ti_1Si_{16}^-$, for which the higher energy isomer (0.06 eV above the lowest-energy one) is the more probable cluster species detected in the experiment.

For bi-doped Si clusters, the density of electronic states near the Fermi level is more complicated than that for the mono-doped systems, giving broadened features in the PES data and making definitive identification more difficult. For $Ti_2Si_{14}^-$ and $Ti_2Si_{15}^-$, the experimental spectrum reveals a low-intensity X (X') peak at 3.04 and 2.98 (3.25) eV, and an A band at 3.52 and 3.52 eV, respectively, followed by a broad high-intensity peak (here assigned as B band) centered at about 4.26 eV (Fig. 2b). The simulated PES of three isomers of $Ti_2Si_{14}^-$ display a first peak with VDE of 3.27, 3.17 and 3.05 eV, respectively. Among them, the third one shows good accordance with the experimental PES, while the simulated PES of the first two isomers of $Ti_2Si_{14}^-$ deviate from the experimental observation. The simulated

Table 2 Natural population analysis of the lowest-energy of $Ti_mSi_n^-$ ($m = 1$–2, $n = 14$–20)

	$Ti_1Si_{14}^-$	$Ti_1Si_{15}^-$	$Ti_1Si_{16}^-$	$Ti_1Si_{17}^-$	$Ti_1Si_{18}^-$	$Ti_1Si_{19}^-$	$Ti_1Si_{20}^-$
<Si>	0.16	0.15	0.14	0.08	0.06	0.07	0.06
Ti	− 3.28	− 3.25	− 3.18	− 2.42	− 2.09	− 2.29	− 2.23
	$Ti_2Si_{14}^-$	$Ti_2Si_{15}^-$	$Ti_2Si_{16}^-$	$Ti_2Si_{17}^-$	$Ti_2Si_{18}^-$	$Ti_2Si_{19}^-$	$Ti_2Si_{20}^-$
<Si>	0.14	0.17	0.09	0.11	0.11	0.09	0.15
Ti1	− 2.88	− 2.98	− 1.84	− 1.83	− 1.81	− 0.79	− 1.99
Ti2	− 0.12	− 0.09	− 0.58	− 1.04	− 1.06	− 1.51	− 1.96

<Si>: the average of Si natural charges, Ti1 is the center atom and Ti2 is the exposed atom. All quantities are in the unit of *e*

PES of 15–I exhibits multiple peaks with the first and second peaks at 3.31 and 3.74 eV, in good accordance with the experimental X' and A bands, respectively. The 15–II isomer has two low-intensity peaks at 3.17 and 3.35 eV, followed by a broad peak above 4.0 eV, coinciding with the experimental X, X' and B bands, respectively. Therefore, we speculate that these two isomers with their small energy difference (only 0.01 eV at 0 K) may coexist in the experiment. Indeed, the calculated free energies of $Ti_2Si_{15}^-$–I and $Ti_2Si_{15}^-$–II isomers (with inclusion of zero-point energy and vibrational entropy effect) would lead to a crossover at a temperature around 80 K.

For $Ti_2Si_{16}^-$, the experimental spectrum reveals X and A peaks at 3.40 and 3.90 eV, respectively, followed by a broad high-intensity peak centered at about 4.25 eV. The simulated PES of two isomers of $Ti_2Si_{16}^-$ display a first peak with VDE of 3.44 and 3.09 eV, respectively. Among them, the 16–I shows good accordance with the experimental PES, while the 16–II deviates from the experimental observation. For $Ti_2Si_{17}^-$ and $Ti_2Si_{18}^-$, the experimental spectrum shows a low-intensity and barely resolved X band at 3.32 and 3.57 eV, overlapping with an A band at 3.58 and 3.76 eV, respectively, along with broad high-intensity peaks above 4.1 eV. The simulated spectrum of 17–I (18–I) isomer displays X and A peaks at 3.32 (3.57) and 3.66 (3.78) eV, respectively, followed by higher peaks in the energy region above 4.1 eV, in agreement with the experimental observation. Therefore, the 17–I and 18–I isomers are probable structures detected in the experiment. The 17–II and 18–II isomers, on the other hand, have higher energies by 0.20 and 0.17 eV than the ground states, respectively, and their simulated spectra are distinct from the experimental ones.

3.3 Bonding and electronic properties of $Ti_mSi_n^-$

To better understand the bonding nature of the $Ti_mSi_n^-$ clusters, we examined the natural charge, bond length, bond order, and binding energies of the ground state configurations which have been identified by the experimental and computed PES. As revealed in Table 2, for the mono-doped Si clusters, the endohedral Ti atom gains 2.09–3.28 *e* from the Si atoms. Generally speaking, the amount of electrons transferred to the Ti atom decreases as the cluster grows bigger due to the increasing Ti–Si bond length (from 2.73 to 2.89 Å); accordingly, the Ti–Si bond order reduces from 0.62 to 0.52, as displayed in Fig. 4a. On the contrary, the Si–Si bond length decreases from 2.54 to 2.45 Å and the bond order increases from 0.44 to 0.71 as the cluster size increases, showing a mixed covalent-metallic bond nature.

For the bi-doped Si clusters, the central Ti atom gains 0.79–2.98 *e* from the Si atoms, while a smaller amount of electrons transfers to the Ti atom on the cluster surface. As n increases

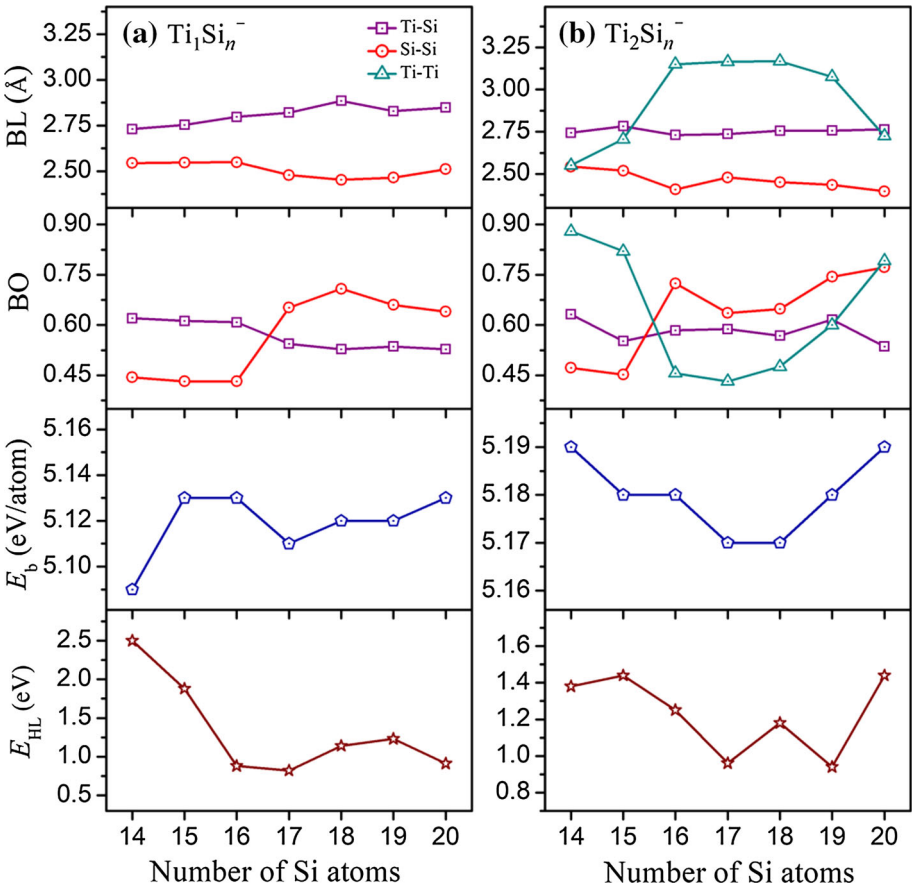

Fig. 4 Average Ti–Si, Si–Si, and Ti–Ti bond lengths (BL), Wiberg bond orders (BO), binding energies (E_b) and HOMO–LUMO gap (E_{HL}) for the ground state structures of $Ti_mSi_n^-$ ($m=$ 1–2, $n=$ 14–20) cluster as a function of the number of Si atoms. The left column and right column correspond to $m=$ 1, and $m=$ 2, respectively. The purple squares, red dot, and cyan triangles correspond to the Ti–Si, Si–Si, and Ti–Ti bond, respectively

and the emerging sub-cage become larger, the natural charge decreases for the central Ti atom and increases for the surface Ti atom. For $Ti_2Si_{20}^-$ with its fused-cage configuration, the two Ti atoms are equivalent and carry almost identical charges (~2.0 *e*). The average Ti–Si bond length varies little (2.72–2.76 Å), whereas the Si–Si bond length decreases from 2.54 to 2.40 Å and the bond order increases from 0.47 to 0.77 as the cluster size increases, due to the transformation of the cage structure to the $Ti@Si_{14}$-based structure. In cage structures, the Ti–Ti bond lengths are 2.55–2.71 Å, very close to the Si–Si bond lengths, which implies that the exposed Ti atoms play the role of Si atoms. With the excess Si atoms attaching to the surface Ti atom, the Ti–Ti bonds lengths are elongated to 3.08–3.17 Å; when the two Ti atoms are encapsulated by fused cages at size 20, the Ti–Ti bond length is 2.68 Å. The Ti–Ti bond lengths in cage-like structures are much longer than the measured Ti–Ti bond length of 1.94 Å in a Ti dimer, and shorter than the nearest neighboring distance of 2.89 Å in the bulk Ti solid [60, 61], while Ti–Ti bond lengths in the $Ti@Si_{14}$-based structures are substantially

longer than both two values. This suggests a stronger interaction between the two Ti atoms in cage-like structures than that in $Ti@Si_{14}$-based structures. The Wiberg bond order of Ti–Ti bonds is 0.79–0.88 in cage-like structures ($n=$ 14–15, 20) and 0.43–0.60 in $Ti@Si_{14}$-based structures ($n=$ 16–19), respectively, in line with the trend of the Ti–Ti bond lengths.

The binding energy of $Ti_1Si_n^-$ clusters increases with size for $n=$ 14–16 (5.09–5.13 eV/atom), decreases again at $n=$ 17 (5.11 eV/atom), then rises slowly with size for $n=$ 18–20 (5.12–5.13 eV/atom). The local minimum ($n=$ 17) corresponds to the formation of the $Ti@Si_{14}$ motif. The local maxima found at $Ti_1Si_{15}^-$ and $Ti_1Si_{16}^-$ designate their high stabilities, which is consistent with the experimental mass spectra showing abundant $Ti_1Si_{15}^-$ and $Ti_1Si_{16}^-$ [27]. The $Ti_1Si_{17}^-$ cluster with hanging Si buds has lower binding energy, and the binding energy increases with n as the Si bud evolves into a sub-cage. For the $Ti_2Si_n^-$ clusters, the binding energy decreases as the cluster grows bigger for $n=$ 14–18 (5.19–5.17 eV/atom) due to the increasing number of attached Si atoms. For $n=$ 19–20, the attached Si atoms start to evolve into a sub-cage, and hence the binding energy rises slightly with n, i.e., 5.18–5.19 eV/atom.

The HOMO–LUMO gap of the $Ti_1Si_n^-$ clusters reduces as cluster size increases from 2.50 to 0.75 eV. As an exception, the $Ti_1Si_{16}^-$ anion has a small HOMO–LUMO gap of 0.75 eV ascribed to the occupancy of SOMO. Generally speaking, the smaller-sized $Ti_1Si_n^-$ clusters ($n=$ 14–15) with cage-like structures possess larger HOMO–LUMO gaps than the larger size ones ($n=$ 17–20) with $Ti@Si_{14}$-based structures. The $Ti_2Si_n^-$ clusters have smaller HOMO–LUMO gap than that of $Ti_1Si_n^-$. As the cluster size increases, the gap decreases for $n=$ 14–17 from 1.38 to 0.95 eV, and then increases with n due to the formation of fused cages.

3.4 Ti_1Si_{16} and Ti_2Si_{15} as superatoms

The minimum VDE values appeared at $Ti_1Si_{16}^-$ and $Ti_2Si_{15}^-$ for $m=1$ and $m=2$, respectively (shown in Fig. 3), which inspire us to study if the $Ti_2Si_{15}^-$ anion has an electron occupying on the SOMO and the corresponding neutral one has a closed electronic shell structure similar to the neutral Ti_1Si_{16} cluster. To confirm this hypothesis and gain further insights, we examine the electronic structures of the neutral Ti_1Si_{16} and Ti_2Si_{15} clusters, which are acquired by fully optimizing the structures of various isomers of $Ti_1Si_{16}^-$ and $Ti_2Si_{15}^-$ anions. The obtained neutral clusters have almost identical structures as their anionic counterparts, except that the outer Ti atom exchanges with an apical Si atom in the distorted FK isomer (Ti_2Si_{15}–III). The FK and distorted FK isomers of neutral Ti_1Si_{16} (Ti_1Si_{16}–I and Ti_1Si_{16}–II), as well as the FK and distorted FK isomers of neutral Ti_2Si_{15} (Ti_2Si_{15}–II and Ti_2Si_{15}–III) are nearly degenerate (energy difference less than 0.07 eV, see Table S1 of Supporting Information). The $Ti@Si_{14}$-based structure of Ti_2Si_{15} (Ti_2Si_{15}–I) is energetically less favorable than the FK isomer by 0.21 eV.

The energy levels and spatial distributions of the occupied molecular orbitals of these two neutral clusters (including ground state configuration and metastable isomers) are illustrated in Fig. 5 and Fig. S4 of Supporting Information. Both neutral $Ti_1Si_{16}^-$ and Ti_2Si_{15} clusters in their ground state behave as superatoms with orbitals can be clearly categorized into superatomic orbitals, leading to a closed electronic shell configuration $(1S)^2(1P)^6(1D)^{10}(1F)^{14}(2S)^2(2P)^6(1G)^{18}(2D)^{10}$. Obviously, the HOMO of the Ti_1Si_{16} cluster has 2D character, while its LUMO corresponds to a 1H orbital. Similar behavior is found for the bi-doped Si cluster as shown in Fig. 5b. Although the orbital energy sequences may be slightly different from each other, their overall electronic configurations are the same. The calculated HOMO–LUMO gaps are 2.98 eV for Ti_1Si_{16} and 1.23 eV for Ti_2Si_{15},

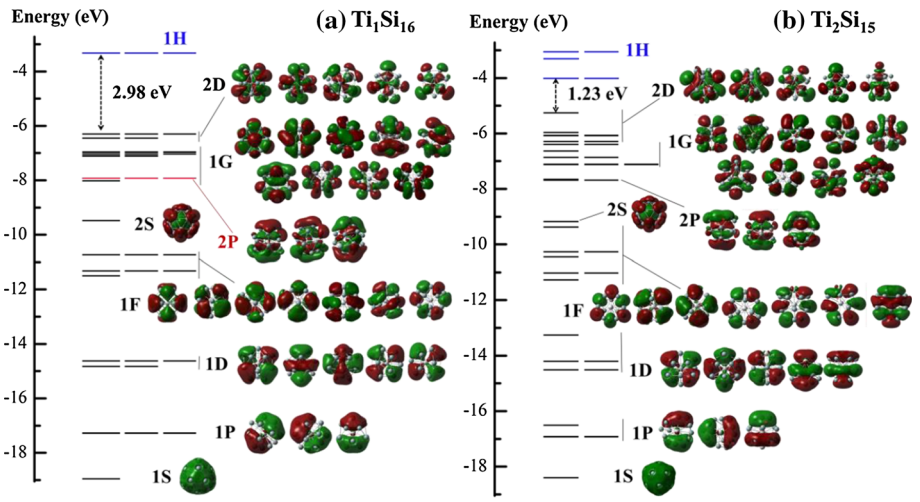

Fig. 5 Energy levels and superatom orbitals for the FK isomers of **a** Ti_1Si_{16} and **b** Ti_2Si_{15}. The number of horizontal line corresponds to the degeneracy of energy level. The HOMO–LUMO gaps are labeled on the corresponding level in the unit of eV. The unoccupied orbitals are indicated in blue

respectively, both suggesting rather high chemical stability. Despite of its relatively smaller HOMO–LUMO gap, the discovery of Ti_2Si_{15} superatom suggests that both Ti atoms contribute four electrons for electron counting of electronic shell.

4 Conclusions

A systematic investigation of the structural and electronic properties of anionic $Ti_mSi_n^-$ ($m=$ 1–2, $n=$ 14–20) clusters have been performed using DFT calculations at the HSE06/aug-cc-pVDZ level of theory, combined with experimental photoelectron spectroscopy. The ground states are identified by comparing the experimental and simulated photoelectron spectra. For $Ti_1Si_n^-$ clusters, the smaller sized clusters ($n=$ 14–16) have cage structure with Ti atoms embedded in the center, while larger size clusters ($n=$ 17–20) adopt the $Ti@Si_{14}$ motif capped by apical Si buds. For $Ti_2Si_n^-$ clusters, the smaller sized clusters ($n=$ 14–15) have cage structure with one Ti atoms encapsulated in the center and the other Ti atom staying on the cluster surface; while for $n=$ 16–20, the $Ti@Si_{14}$-based structure starts to dominate the low-lying isomers and the excess Si atoms start to evolve into a sub-cage enclosing the Ti atom on the cluster surface. Natural population analysis reveal that the Ti atoms possess negative charges acting as electron acceptors in all clusters, while less amount of electron is transferred to the surface Ti atom. The neutral Ti_1Si_{16} and Ti_2Si_{15} clusters are identified as superatoms with closed electronic shells of $(1S)^2(1P)^6(1D)^{10}(1F)^{14}(2S)^2(2P)^6(1G)^{18}(2D)^{10}$. Except for the Ti_1Si_{16} cluster, the newly found Ti_2Si_{15} cluster with closed electronic shells and high stability may also suitable as building blocks for novel nanomaterials.

Acknowledgements We would like to express thanks to Prof. Vijay Kumar for stimulating discussion. This work was supported by the National Natural Science Foundation of China (91961204, 11974068 and 11804076), the Key Project of Natural Science Foundation of Tianjin City (No. 17JCZDJC30100), the Fundamental Research Funds for the Central Universities of China (DUT20LAB110 and DUT20LAB203), and the Supercomputing Center of Dalian University of Technology.

References

1. J.J. Zhao, Q.Y. Du, S. Zhou, V. Kumar, Chem. Rev. (2020). https://doi.org/10.1021/acs.chemrev.9b00651
2. M.F. Jarrold, Science **252**, 1085 (1991)
3. S.N. Khanna, P. Jena, Phys. Rev. B **51**(19), 13705 (1995)
4. V. Kumar, Y. Kawazoe, Phys. Rev. Lett. **87**(4), 045503 (2001)
5. S.N. Khanna, B.K. Rao, P. Jena, Phys. Rev. Lett. **89**(1), 016803 (2002)
6. V. Kumar, T.M. Briere, Y. Kawazoe, Phys. Rev. B **68**(6), 155412 (2003)
7. U. Röthlisberger, W. Andreoni, M. Parrinello, Phys. Rev. Lett. **72**(5), 665 (1994)
8. C.L. ReisJ, M. Pacheco, J. Phys. Condens. Matter **22**(3), 035501 (2010)
9. C.L. Reis, J.M. Pacheco, Phys. Rev. B **82**(15), 155440 (2010)
10. J. Wang, Q.M. Ma, R.P. Xu, Y. Liu, Y.C. Li, Phys. Lett. A **373**(32), 2869 (2009)
11. H. Tsunoyama, H. Akatsuka, M. Shibuta, T. Iwasa, Y. Mizuhata, N. Tokitoh, A. Nakajima, J. Phys. Chem. C **121**, 20507 (2017)
12. K. Koyasu, M. Akutsu, M. Mitsui, A. Nakajima, J. Am. Chem. Soc. **127**(14), 4998 (2005)
13. X. Huang, S.J. Lu, X. Liang, Y. Su, L. Sai, Z.G. Zhang, J. Zhao, H.G. Xu, W. Zheng, J. Phys. Chem. C **119**(20), 10987 (2015)
14. S. Neukermans, X. Wang, N. Veldeman, E. Janssens, R.E. Silverans, P. Lievens, Int. J. Mass Spectrom. **252**(2), 145 (2006)
15. K. Koyasu, J. Atobe, M. Akutsu, M. Mitsui, A. Nakajima, J. Phys. Chem. A **111**(1), 42 (2007)
16. H. Kawamura, V. Kumar, Y. Kawazoe, Phys. Rev. B **71**(7), 075423 (2005)
17. L.J. Guo, X. Liu, G.F. Zhao, Y.H. Luo, J. Chem. Phys. **126**(23), 234704 (2007)
18. A. Willand, M. Gramzow, S.A. Ghasemi, L. Genovese, T. Deutsch, K. Reuter, S. Goedecker, Phys. Rev. B **81**(20), 201405 (2010)
19. N.A. Borshch, N.S. Pereslavtseva, S.I. Kurganskii, Russ. J. Phys. Chem. **88**(10), 1512 (2014)
20. C. Dong, L. Han, J. Yang, L. Cheng, Int. J. Quantum Chem. **119**(18), e25978 (2019)
21. D. Bandyopadhyay, J. Appl. Phys. **104**(8), 084308 (2008)
22. D. Bandyopadhyay, M. Kumar, Chem. Phys. **353**(1), 170 (2008)
23. W. Pei, S. Zhou, Y. Bai, J. Clust. Sci. **31**, 627 (2020)
24. P. Sen, L. Mitas, Phys. Rev. B **68**(68), 155404 (2003)
25. T. Iwasa, A. Nakajima, J. Phys. Chem. C **116**(26), 14071 (2012)
26. M.I.A. Oliveira, R. Rivelino, F.D.B. Mota, G.K. Gueorguiev, J. Phys. Chem. C **118**(10), 5501 (2014)
27. M. Ohara, K. Koyasu, A. Nakajima, K. Kaya, Chem. Phys. Lett. **371**(3), 490 (2003)
28. S. Furuse, K. Koyasu, J. Atobe, A. Nakajima, J. Chem. Phys. **129**(6), 064311 (2008)
29. K. Koyasu, J. Atobe, S. Furuse, A. Nakajima, J. Chem. Phys. **129**(21), 214301 (2008)
30. M.B. Torres, E.M. Fernández, L.C. Balbás, J. Comput. Methods Sci. Eng. **7**(3,4), 241 (2007)
31. J.U. RevelesS, N. Khanna, Phys. Rev. B **74**(3), 035435 (2006)
32. J. He, K. Wu, C. Liu, R. Sa, Chem. Phys. Lett. **483**(1–3), 30 (2009)
33. M.B. Torres, E.M. Fernández, L.C. Balbás, Phys. Rev. B **75**(75), 205425 (2007)
34. L.J. Guo, G.F. Zhao, Y.Z. Gu, X. Liu, Z. Zeng, Phys. Rev. B **77**(77), 195417 (2008)
35. J. Zhao, R. Shi, L. Sai, X. Huang, Y. Su, Mol. Simul. **42**(10), 809 (2016)
36. B. Delley, J. Chem. Phys. **113**(18), 7756 (2000)
37. L.W. Sai, X. Wu, X.M. Huang, J.J. Zhao, J. Clust. Sci. **28**(3), 1729 (2017)
38. X. Wu, X. Liang, Q. Du, J. Zhao, M. Chen, M. Lin, J. Wang, G. Yin, L. Ma, R.B. King, B.V. Issendorff, J. Phys. Condens. Matter **30**, 354002 (2018)
39. L.W. Sai, X. Wu, N. Gao, J.J. Zhao, R.B. King, Nanoscale **9**, 13905 (2017)
40. X. Wu, L. Sai, S. Zhou, P. Zhou, M. Chen, M. Springborg, J. Zhao, Phys. Chem. Chem. Phys. **22**, 12959 (2020)
41. X. Huang, H.G. Xu, S. Lu, Y. Su, R.B. King, J. Zhao, W. Zheng, Nanoscale **6**(24), 14617 (2014)
42. X. Wu, S.-J. Lu, X. Liang, X. Huang, Y. Qin, M. Chen, J. Zhao, H.-G. Xu, R.B. King, W. Zheng, J. Chem. Phys. **146**(7), 044306 (2017)
43. X. Wu, S. Zhou, X. Huang, M. Chen, R.B. King, J. Zhao, J. Comput. Chem. **39**, 2268 (2018)
44. X.Q. Liang, X.J. Deng, S.J. Lu, X. Huang, J. Zhao, H.G. Xu, W.J. Zheng, X.C. Zeng, J. Phys. Chem. C **121**, 7037 (2017)
45. X. Liang, X. Kong, S.-J. Lu, Y. Huang, J. Zhao, H.-G. Xu, W. Zheng, X.C. Zeng, J. Phys. Condens. Matter **30**, 335501 (2018)
46. Y. Wang, X. Wu, J. Zhao, J. Clust. Sci. **29**, 847 (2018)
47. J.P. Perdew, K. Burke, M. Ernzerhof, Phys. Rev. Lett. **77**(18), 3865 (1996)
48. J.P. Perdew, K. Burke, M. Ernzerhof, Phys. Rev. Lett. **78**, 1396 (1997)

49. M. J. Frisch, G. W. Trucks, H. B. Schlegel, G. Scuseria, M. Robb, J. Cheeseman, G. Scalmani, V. Barone, B. Mennucci, G. Petersson, *Gaussian 09, Revision A.1* (Gaussian Inc., Wallingford, 2009)
50. T.H. Dunning Jr, J. Chem. Phys. **90**(2), 1007 (1989)
51. A.V. Krukau, O.A. Vydrov, A.F. Izmaylov, G.E. Scuseria, J. Chem. Phys. **125**(21), 224106 (2006)
52. C. Adamo, J. Chem. Phys. **110**(13), 6158 (1999)
53. A.E. Reed, R.B. Weinstock, F. Weinhold, J. Chem. Phys. **83**(2), 735 (1985)
54. A.E. Reed, L.A. Curtiss, F. Weinhold, Chem. Rev. **88**(6), 899 (1988)
55. J.E. Carpenter, F. Weinhold, J. Mol. Struct. Theochem **169**(4), 41 (1988)
56. D.J. TozerN, C. Handy, J. Chem. Phys. **109**(23), 10180 (1998)
57. J. Akola, M. Manninen, H. HäKkinen, U. Landman, X. Li, L.S. Wang, Phys. Rev. B **62**(19), 13216 (2000)
58. L. Ma, B.V. Issendorff, A. Aguado, J. Chem. Phys. **132**(10), 104303 (2010)
59. F.C. FrankJ, S. Kasper, Acta Cryst. **11**(3), 184 (1958)
60. R.W.G. Wyckoff, *Crystal Structures* (Interscience Publishers, New York, 1963)
61. M. Doverstal, B. Lindgren, U. Sassenberg, C.A. Arrington, M.D. Morse, J. Chem. Phys. **97**(10), 7087 (1992)